iScience

Article

Scalable one-pot synthesis of aminated reduced graphene oxide for high-performance supercapacitor electrodes

Graphical abstract

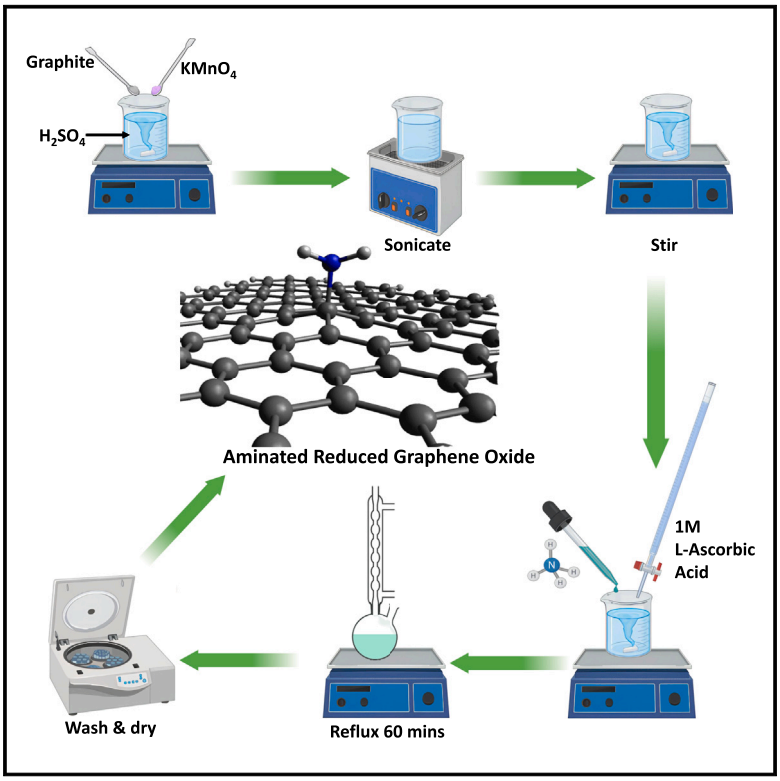

Highlights

- It is one of the fastest methods for synthesizing aminated reduced graphene oxide
- The process allows for tunable nitrogen content and customizable C:O ratios
- Fabricated symmetric supercapacitor exhibited an energy density of 54.18 Wh kg^{-1}
- The supercapacitor showed 98% charge retention after 10,000 cycles

Authors

Suraj Kumar, Priyakshi Bora, Kunal Roy, Navya Rani M., Dinesh Rangappa, Dipak Sinha

Correspondence

dinesh.rangappa@vtu.ac.in (D.R.), dipaksinha@gmail.com (D.S.)

In brief

Electrochemical energy storage; Chemical synthesis; Energy materials

Kumar et al., 2025, iScience *28*, 112271
April 18, 2025
https://doi.org/10.1016/j.isci.2025.112271

CellPress

iScience

CellPress
OPEN ACCESS

Article

Scalable one-pot synthesis of aminated reduced graphene oxide for high-performance supercapacitor electrodes

Suraj Kumar,[1] Priyakshi Bora,[1] Kunal Roy,[2] Navya Rani M.,[3] Dinesh Rangappa,[2,*] and Dipak Sinha[1,4,*]
[1]Department of Chemistry, School of Sciences, Nagaland University, Zunheboto, Nagaland 798627, India
[2]Department of Applied Sciences (Nanotechnology), Centre for Post-Graduate Studies, Visvesvaraya Technological University, Muddenahalli, Karnataka 562101, India
[3]Centre for Research and Development, Nagarjuna College of Engineering and Technology, Bengaluru, Karnataka 562164, India
[4]Lead contact
*Correspondence: dinesh.rangappa@vtu.ac.in (D.R.), dipaksinha@gmail.com (D.S.)
https://doi.org/10.1016/j.isci.2025.112271

SUMMARY

Functionalizing graphene by adding amine groups can significantly enhance its wettability and overall properties. However, traditional methods for introducing $-NH_2$ typically require lengthy processing times, high temperatures, and pressures, which limit their suitability for large-scale production. This work presents the fastest method reported to date for synthesizing aminated reduced graphene oxide (NH_2-rGO) under moderate temperatures, completing the entire process in just ~9 h. The nitrogen content of the NH_2-rGO is tunable from 2 to 6% and the material also exhibits excellent electrochemical properties. A symmetric supercapacitor based on the prepared material demonstrated a specific capacitance of 322 F g^{-1} at 1 A g^{-1}, which is a 5-fold increase compared to rGO. It also delivered an impressive volumetric energy density of 48.16 Wh L^{-1}, which is nearly seven times higher than rGO (6.89 Wh L^{-1}). Further, NH_2-rGO could also be utilized in biosensing, photovoltaics, catalysis, and as a base for further chemical modifications.

INTRODUCTION

The increasing reliance on non-renewable energy sources, from individual households to large-scale industries, highlights the pressing need for advanced energy storage solutions. These devices enable efficient storage of energy from renewable sources, such as sunlight, wind, ensuring its availability for future use. Despite variations in their methods of storing and delivering energy, most energy storage devices share a common purpose: to store charge.[1] Among these, supercapacitors stand out for their ability to rapidly store and discharge energy.[2] Supercapacitors store energy through two main mechanisms: electrical double-layer (EDL) capacitance and pseudocapacitance. EDL capacitors utilize electrode materials with a high surface area, where energy is stored through the accumulation of charges at the interface between the electrode and electrolyte. Since EDL-based supercapacitors do not involve physical changes in the electrodes during operation, they can sustain millions of charge and discharge cycles with minimal degradation in performance.[2] Pseudocapacitors, on the other hand, store energy via reversible Faradaic redox reactions. Materials with pseudocapacitive properties, such as MXenes, polyaniline offer significantly higher energy densities compared to EDL-based supercapacitors. However, the Faradaic reactions occurring in pseudocapacitive electrodes can cause phase changes, which may reduce their lifespan and power density.[3,4] Additionally, EDL capacitors have faster response times compared to pseudocapacitors, making them better suited for applications that require rapid energy storage and release.[4]

A highly promising electrode material for EDL capacitors is graphene, a 2D allotrope of carbon with sp^2-hybridized carbon atoms arranged in a hexagonal lattice.[5] Its exceptional optical, mechanical, and electrical properties have generated significant interest, fueling the advancement of numerous applications.[2,6] These include drug delivery,[7] biochemical and electrochemical sensors,[8] optoelectronic and microelectronic devices,[9] and energy storage devices.[10] Although graphene possesses remarkable properties, its widespread use has been hindered by difficulties in large-scale production and its limited reactivity due to the lack of functional groups on its surface.[11,12] However, recent progress in the mass production of graphene and its derivatives, including graphene oxide (GO), reduced graphene oxide (rGO), and functionalized graphene nanosheets, has helped to overcome many of these challenges.[13–15] Chemically modified and functionalized graphene has become a key focus of research in graphene-based materials, particularly for applications in supercapacitors.[16–21] The growing interest in graphene functionalization stems from the potential to tailor its physical and chemical properties by adding specific organic groups to either the basal plane or the edges of graphene. Studies suggest that incorporating chemically reactive species, like amines,[22,23] modifies the reactivity and chemistry of graphene's surface,

thereby tremendously increasing the performance of graphene-based catalysts, energy storage devices, gas sensors, and biosensors.[24–26] Additionally, functionalization aids in the effective dispersion of graphene in common solvents, tackling a major difficulty in processing graphene-based materials.[27] As a result, significant efforts are being made to covalently modify graphene with various functional groups, thereby considerably expanding the family of functionalized graphenes.

Nitrogen is a common heteroatom that can be introduced into graphene through thermal treatment to enhance its performance in supercapacitors.[28–30] However, the high-temperature treatment typically results in the formation of nitrogen functionalities, such as pyrrolic, pyridinic, quaternary, or pyridinic-N-oxides.[12,31,32] While these nitrogen substitutions enhance performance, they can also lead to poor wettability and chemical reactivity, which require further chemical modifications. Unlike nitrogen substitution, primary amines can be introduced into graphene sheets as ionizable functional groups, which could further improve the supercapacitor's electrochemical properties.[12] These ionizable groups have the potential to enhance the uniform and stable dispersion of graphene, facilitating its assembly or interaction with various polymers, organic molecules, and biological systems, including DNA as well as fullerenes or carboxylated carbon nanotubes.[11,12,33] Furthermore, due to the electron-withdrawing tendency of amines, functionalizing graphene with amines alter the electronic structure, enhancing conductivity and allowing for precise engineering of work function.[34] As a result, aminated graphene is considered a suitable material for numerous fields ranging from drug delivery, photovoltaics, sensing, and energy storage.[12,35–37]

Several approaches have been developed to prepare aminated reduced graphene oxide (NH_2−rGO). For instance, Lai et al.[12] demonstrated successful functionalization with primary amines through a single-step solvothermal process, utilizing ethane-1,2-diol as the solvent and ammonia as the nitrogen source. However, the process takes >200 h, involves multiple steps, and operates at a high temperature of 180°C for 10 h. Furthermore, an analysis of the X-ray diffraction (XRD) data reveals that the characteristic features of GO are retained, indicating incomplete reduction. Similarly, Zhang and colleagues[37] produced amino-functionalized graphene oxide through Hoffman rearrangement, starting with GO and achieving an amine concentration of ∼4%. The reaction takes ∼47 h and involves multiple steps, making it unsuitable for large-scale production. In another report, Rabchinskii et al.[32] synthesized aminated reduced graphene oxide following a two-step process. GO was initially brominated with hydrobromic acid followed by subsequent treatment with ammonia, yielding ∼4% amination degree. However, this method makes use of toxic chemicals, entails the use of high temperatures, is time-consuming (∼70 h), has multiple steps, and requires additional processing. Furthermore, using high temperatures results in the inclusion of nitrogen-containing heterocycles, such as pyrroles, quaternary, or pyridinic-N-oxides and pyridines rather than the formation of amines.[12] Therefore, there is a growing demand for environmentally friendly methods that enable high-yield synthesis of NH_2−rGO, at a reasonable cost for various applications. These methods not only need to be cost-effective but also sustainable, aligning with the current push toward greener technologies and practices in material production. As a result, researchers are focused on developing efficient, scalable, and eco-friendly approaches to meet these rising industrial demands.

In light of the aforementioned, we report, for the first time, a simple, one-pot, eco-friendly, and scalable method for preparing NH_2−rGO in a record time of approximately 9 h, making it the fastest method reported to date. This approach avoids the use of high temperatures, pressures, and toxic chemicals. It also achieves a high degree of amination (∼6%), with the nitrogen content controllable by adjusting the pH of the reaction mixture (RM). The success of this method has been confirmed through X-ray photoelectron spectroscopy (XPS), Fourier transform infrared (FTIR), and energy dispersive spectroscopy (EDS). The surface morphology of the NH_2−rGO was analyzed using scanning electron microscopy (SEM). Furthermore, the incorporation of amine groups enhances the wettability of rGO, making it an excellent electrochemical material. The effect of this functionalization has been systematically studied to evaluate the potential of NH_2−rGO as supercapacitor electrodes. Variants of NH_2−rGO—namely A-5, A-7, A-9, and A-12 (see synthesis of NH_2−rGO section for the adopted nomenclature in this work)—show significant improvements compared to unfunctionalized rGO.

The symmetric supercapacitor fabricated with our as-synthesized material demonstrated (1) a significantly higher specific capacitance compared to rGO and similar materials, (2) exceptional charge-discharge cycling stability, with around 98% capacitance retention after 10,000 cycles of continuous operation, and (3) remarkable improvements in both gravimetric and volumetric energy and power densities, surpassing those of rGO by many folds and even outperforming some binary composites. Additionally, the use of the ionic liquid 1-ethyl-3-methylimidazolium tetrafluoroborate ($EMIMBF_4$) in acetonitrile allowed us to overcome the limited electrochemical window of water-based electrolytes, expanding the operating voltage window to 2.2 V and thereby enhancing the potential for practical applications.

RESULTS AND DISCUSSION

Chemical composition analysis

XPS was employed to analyze the chemical composition of the NH_2−rGO samples. It is a widely used technique for analyzing the surface chemical structure of graphene, especially in samples that have been chemically modified.[38] The survey spectra of all NH_2−rGO samples, shown in Figure 1A, exhibit C1s, N1s, and O1s peaks at binding energies of ∼284 eV, ∼399 eV, and ∼532 eV, respectively. The peak at ∼399 eV confirms the successful incorporation of nitrogen species into all samples. The atomic concentrations for the samples are depicted in Figure 1B. The C:O ratios for all the samples are greater than GO (∼1.7:1),[12] which indicates successful deoxygenation/reduction during the reaction, aligning with the XRD results. Moreover, this implies that the C:O ratio can be regulated by modifying the pH of the RM during synthesis. Additionally, the nitrogen content can be tuned by controlling the pH of the RM. The nitrogen content

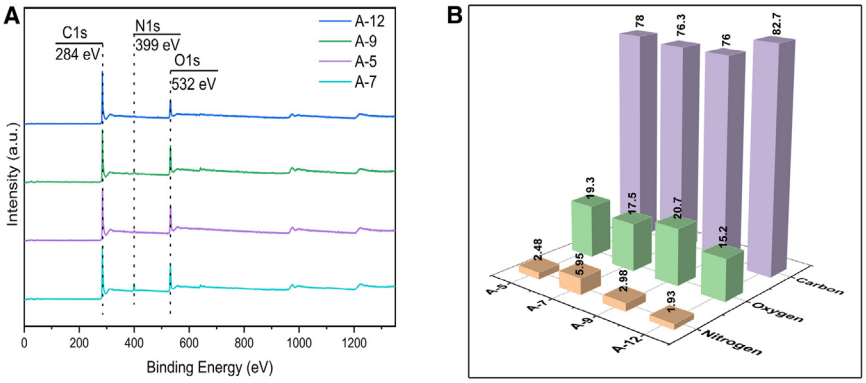

Figure 1. XPS survey spectra and atomic concentrations

(A) XPS survey spectra of A-5, A-7, A-9, and A-12.
(B) Atomic concentrations of A-5, A-7, A-9, and A-12 obtained from XPS.

increased from 2.48% for A-5 to 5.95% for A-7 and then decreased to 2.98% for A-9 and 1.93% for A-12. Thus, the amination degree is strongly influenced by the pH of the RM, indicating that a highly basic condition is not favorable for amine grafting.[12] The diminished ability of ammonia to adsorb onto the graphite sheets in the RM in an alkaline environment might be the primary cause for the reduced incorporation of nitrogen species.[12,39]

Furthermore, in order to differentiate whether the observed nitrogen is connected to graphene through covalent bonds or merely adhered to its surface through physisorption, high-resolution C1s and N1s spectra were recorded and deconvoluted. As shown in Figures 2A–2D, the C1s spectrum of all NH_2−rGO samples can be fitted with six components. The component at 284.7 eV is attributed to sp^2-bonded carbons in aromatic domains (C=C).[32] The three peaks at 289.1 eV, 288.2 eV, and 286.7 eV are assigned to COOH, C=O, and C–OH & C–O–C groups, respectively.[12,40–42] Additionally, the component at 285.8 eV in all the samples is attributed to the existence of C–N groups, indicating successful amination.[12,40] The last peak, around 291 eV, is assigned to the $\pi-\pi^*$ shakeup satellite of the C=C peak.[32]

The N1s spectrum of A-7 (Figure 2F) can be deconvoluted into three components with binding energies of 399.8 eV, 401.4 eV, and 403.8 eV, corresponding to primary amines,[43,44] graphitic-N, and pyridinic-O, respectively.[32] The spectrum indicates that amine functionality is the predominant nitrogen species, accounting for 81.32% of the peak area, while graphitic and pyridinic nitrogen species are present in much smaller amounts, at 15.28% and 3.40%, respectively. Similarly, the N1s spectra of A-5, A-9, and A-12 were also deconvoluted as shown in Figures 2E, 2G, and 2H, respectively. It was observed that their N1s spectrum could be broken down into four components: pyridinic-N (398.4 eV), primary amines (399.8 eV), graphitic-N (401.4 eV), and pyridinic-O (403.8 eV). Notably, all the deconvoluted spectra exhibited peaks at 399.8 eV and 401.4 eV corresponding to primary amines and N–C bonds. This indicates the formation of chemical bonds between the nitrogen from the amines and the carbon framework, confirming the actual functionalization of the graphene structures.[45] Table 1 summarizes the concentrations of functional groups obtained by deconvoluting the N1s and C1s spectra of A-5, A-7, A-9, and A-12.

The successful amination is also demonstrated through FTIR spectroscopy. The FTIR spectra of all samples are illustrated in Figures 3A and S1. The bands at 1,400 cm^{-1}, 1,622 cm^{-1}, and 1,732 cm^{-1} can be attributed to C–H/C–H_2 vibrations and C=O in carbonyl and carboxylic acid moieties.[40–42,46] Additionally, in all samples, the characteristic bands of GO at 1,220 cm^{-1}, 1,365 cm^{-1}, and 2,970 cm^{-1} associated with oxygen functionalities and interlayer water either disappear or decrease, indicating successful dehydration and reduction. Moreover, a peak centered at ~3,440 cm^{-1}, along with peaks at 1,580 cm^{-1} and 1,064 cm^{-1} attributed to N–H stretching, N–H bending, and C–N stretching of primary amines, is observed.[32] This indicates successful amination, which aligns with the XPS results.

Study of the morphological features

The structural characteristics of the synthesized NH_2−rGOs were further examined using various techniques, including XRD and SEM. The XRD spectra were measured over a 2θ range (5°–60°) with a scan rate of 0.02°. As shown in Figure 3B, the spectra reveal a (002) diffraction peak around $2\theta \approx 25°$ corresponding to an interlayer spacing of 0.35 nm. This suggests effective reduction and partial disruption of the long-range order typical of graphite, as well as a change in the distance between layers. This disruption is attributed to the incorporation of amino groups during the reduction process, which alters the stacking arrangement of the graphene layers.[47] Additionally, the spectra display a (10) diffraction peak at $2\theta \approx 45°$, indicating the presence of short-range order.[43,48] Importantly, the XRD pattern of all NH_2−rGO samples lacks the characteristic features of GO. This absence of GO peaks indicates the successful reduction of functional groups containing oxygen, such as epoxy and hydroxyl groups. These results align with the findings from XPS and FTIR findings. In contrast, the solvothermal process developed by Lai and Colleagues[12] retains GO features post-reduction suggesting a less complete reduction compared to the present method. This highlights the effectiveness of the current method.

The morphology and elemental composition of the NH_2−rGO samples were also analyzed using SEM and EDS. The SEM images of A-5, A-7, A-9, and A-12 are presented in Figures 3C–3F. The figures reveal that the NH_2−rGO samples are composed of thin sheets that are haphazardly clustered together, forming a wrinkled and twisted structure characteristic of graphene-based materials. This indicates that the applied synthesis method had no significant effect on the morphology.[49] The distribution of nitrogen, oxygen, and carbon in all samples was also quantified by SEM-EDS (Table 2). The elemental composition analysis showed significant variation in nitrogen concentration across

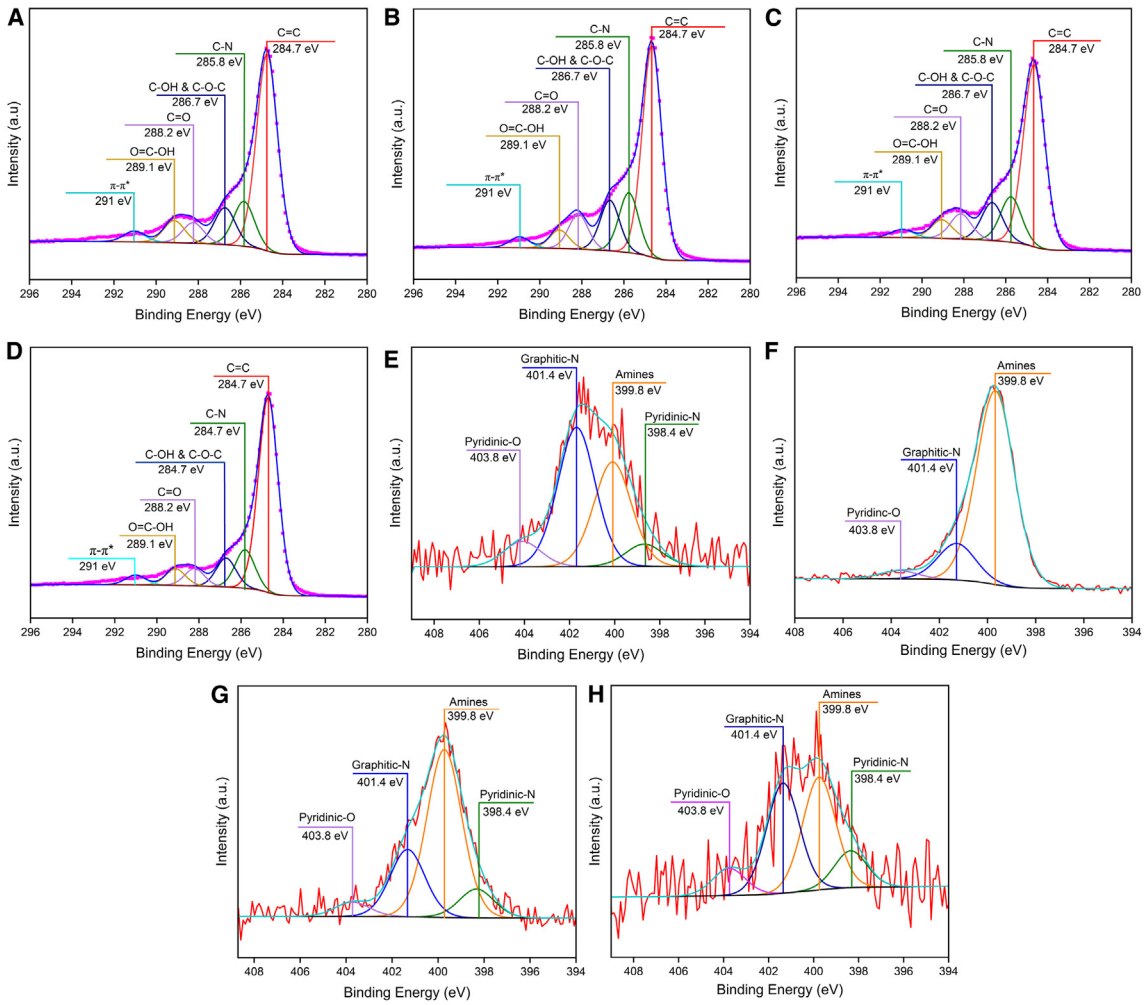

Figure 2. Deconvoluted HR-XPS spectra

(A) C1s region of A-5.
(B) C1s region of A-7.
(C) C1s region of A-9.
(D) C1s region of A-12.
(E) N1s region of A-5.
(F) N1s region of A-7.
(G) N1s region of A-9.
(H) N1s region of A-12.

the samples, with A-7 having the highest nitrogen content (5.01%), followed by A-9 (2.46%), A-5 (2.26%), and A-12 (0.33%). These findings align with the XPS results, which display the same trend. Since A-7 has the highest nitrogen content, element distribution mapping was conducted to examine the distribution of different elements throughout the matrix, as depicted in Figures 3G–3I. The results reveal that nitrogen is uniformly and densely distributed across the carbon matrix, demonstrating that the reaction occurred at both the edges and within the bulk of the matrix. Therefore, the present reported method offers several benefits, including simplicity, cost-effectiveness, reduced reaction time, and high yield, in comparison to other techniques reported in the literature.[12,32]

Electrochemical performance

Graphene and its composites have recently emerged as promising alternatives to traditional carbon electrodes in supercapacitor applications, offering improved performance.[47,50,51] Therefore, considering the potential of NH_2−rGO as an electrode material, we investigated its application in supercapacitors. The electrochemical performance of NH_2−rGO samples, along with rGO for comparison, was initially assessed in a three-electrode cell. Figure 4A shows the cyclic voltammetry (CV) curves of all the samples within the potential range of −0.6 to 1.2 V at 5 mV s^{-1} versus Ag/Ag^+. The CV profiles exhibit a rectangular shape characteristic of electric double-layer capacitance (EDLC), with minor redox peaks likely resulting from the nitrogen and oxygen functional

Table 1. The relative concentrations of some of the functional groups determined by deconvoluted HR-XPS spectra of N1s and C1s regions of NH_2−rGO samples

Component	C=C	C–N	C–OH & C–O–C	C=O	O=C–OH	Pyridinic-N	Primary amines	Graphitic-N	Pyridinic-O
Binding energy (eV)	284.7	285.8	286.7	288.2	289.1	398.4	399.8	401.4	403.8
A-5	61.08	13.99	11.48	6.38	7.01	7.60	35.93	47.85	8.61
A-7	54.77	15.55	13.05	9.08	4.75	0.00	81.32	15.28	3.40
A-9	57.26	14.28	11.96	7.97	5.87	10.36	60.28	24.19	5.18
A-12	63.60	12.62	9.49	5.66	5.44	12.82	39.31	38.39	9.48

groups present, as confirmed by XPS and FTIR analyses.[30,50] Among the samples, A-7 demonstrates the largest enclosed CV area, signifying superior energy storage capability compared to A-5, A-9, A-12, and rGO. The similar CV areas of A-5 and A-9 correlate with their comparable nitrogen content, as determined by XPS and EDS analyses. Meanwhile, A-12, which contains the lowest nitrogen content, exhibits the smallest CV area among the NH_2−rGO samples.

All electrodes exhibited the highest specific capacitance (C_S) at 5 mV s^{-1} and showed a steady decrease as the scan rate increased, which is generally anticipated because of diffusion limitations within the electrode surface's pores (Figure 4B).[52] Notably, A-5, A-7, A-9, and A-12 exhibit capacitance values that are 2.43, 2.85, 2.72, and 1.62 times higher than rGO, highlighting their superior performance. The enhanced performance of NH_2−rGO can be credited to an enhanced ion-accessible surface area, which facilitates better diffusion of ions and quicker ion extraction/insertion.[47,53] To further evaluate the performance of the electrode materials, galvanostatic charge-discharge (GCD) measurements were conducted at various current densities ranging from 1 to 10 A g^{-1}. Figure 4C presents the GCD profiles of all the samples at 1 A g^{-1}, which are quasi-triangular in shape, indicating purely capacitive behavior. The C_S values were calculated from the GCD curves using Equation 2. At 1 A g^{-1}, the C_S values were 1150.20 F g^{-1}, 1573.2 F g^{-1}, 1229.4 F g^{-1}, 894.60 F g^{-1}, and 345.60 F g^{-1} for A-5, A-7, A-9, A-12, and rGO, respectively. Additionally, the variation of C_S with current density is depicted in Figure 4D. There is a noticeable drop in

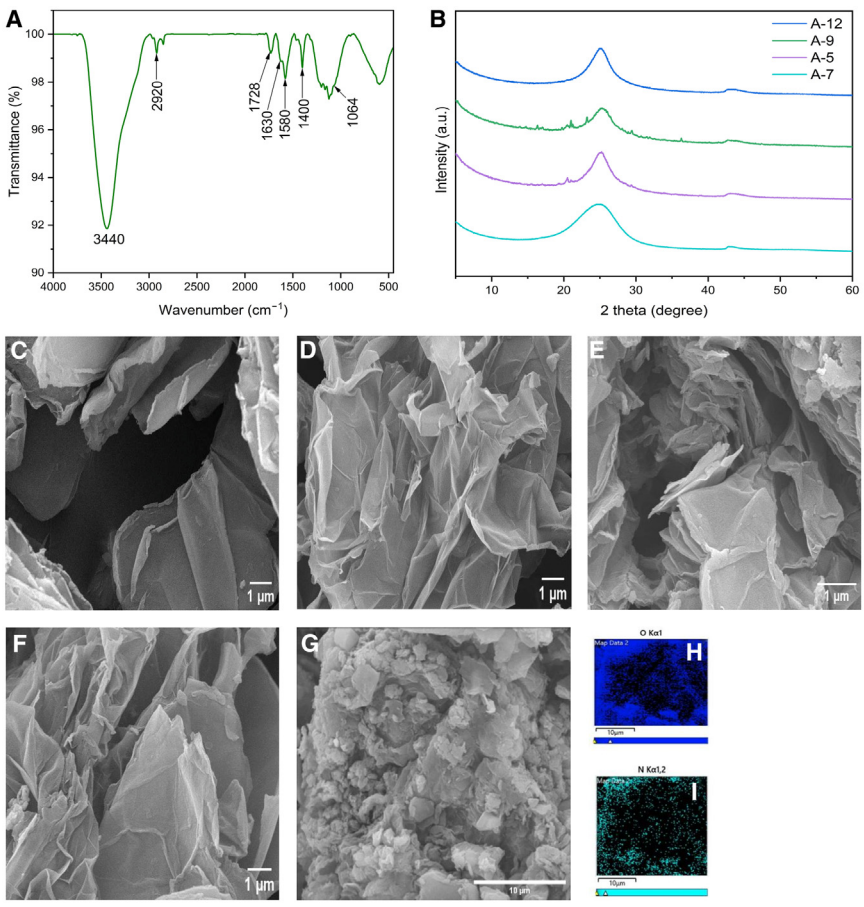

Figure 3. Materials characterization

(A) FTIR spectrum of A-7.

(B) XRD spectra of A-5, A-7, A-9, and A-12.

(C−F) FE-SEM image of (C) A-5, (D) A-7, (E) A-9, and (F) A-12. Scale bars, 1 μm.

(G–I) (G) SEM image of A-7 utilized for elemental mapping, including (H) oxygen map, (I) nitrogen map.

Table 2. Concentration of elements (in at.%) according to EDS

Sample	Carbon	Oxygen	Nitrogen	Other elements
A-5	81.32	2.05	2.05	Sodium (0.11%)
A-7	74.82	18.78	5.01	Sulfur (1.39%)
A-9	82.58	14.95	2.46	Sodium (0.02%)
A-12	86.98	12.69	0.33	–

C_S at lower current densities, followed by a more gradual decline at higher current densities, highlighting the enhanced power capability of NH_2−rGOs. This decrease is likely attributed to reduced ion accessibility to the active surface at higher current densities.[52] Remarkably, A-7 retained a specific capacitance of 432 F g^{-1} at 10 A g^{-1}, nearly five times greater than that of rGO, as shown in Figure 4D. The results indicate a clear trend: as the nitrogen content increases, the electrochemical performance improves, with A-7 emerging as the best-performing electrode, followed by A-9, A-5, and A-12. Thus, the results highlight the potential of NH_2−rGOs, particularly A-7 as an advanced electrode material for supercapacitors. Its superior performance is due to the presence of nitrogen species that improve the surface wettability thereby aiding ion transport across the surface.

To investigate the practical applications of NH_2−rGO, symmetric two-electrode supercapacitor devices were fabricated and tested. Based on its superior performance in the three-electrode system, A-7 was selected as the active material for the symmetric supercapacitor. Two pieces of graphite sheets of dimensions (length = 3 cm, width = 1 cm, thickness = 200 microns) were coated with the active material in a 1 cm × 1 cm area. The coated sheets were separated by grade 1 Whatmann filter paper, which was soaked in 1 M $EMIMBF_4$ in acetonitrile overnight before the fabrication of the device (Figure 5A). For comparison, a symmetric supercapacitor using rGO as the active material was fabricated under identical conditions. These devices were then subjected to performance evaluations to assess their potential for practical applications.

Figure 5B demonstrates the CV curves at a scan rate of 5 mV s^{-1} of the assembled supercapacitors within the 0 to 2.2 V potential window. It can be observed that the CV curves show a rectangular shape, typical of EDLC behavior.[30,54] Further, the rectangular shape was preserved even at scan rates of 100 mV s^{-1} (Figure 5C) for A-7 based symmetric supercapacitor (A-7 SSC), which is an indication that the symmetric supercapacitor demonstrates capacitive behavior with rapid charge transport at the interfaces as well as the material.[55] The C_S computed from the CV curves at different scan rates is presented in Figure 5D. A-7 demonstrated a C_S of 568.69 F g^{-1} at 5 mV s^{-1}, which is a 3.5-fold increase as compared to rGO-based symmetric supercapacitor (rGO SSC) and at 100 mV s^{-1}, A-7 SSC delivered a C_S of 182.10 F g^{-1}, further highlighting the ease of ion access throughout the entire architecture. GCD measurements were also conducted to evaluate the electrochemical performance of the fabricated supercapacitor devices. Figure 5E illustrates the GCD curves of rGO SSC and A-7 SSC at 1 A g^{-1}. Both curves exhibit a triangular profile, indicative of capacitive energy storage behavior, consistent with the trends observed in the CV analysis. Notably, A-7 SSC demonstrated C_S of 322 F g^{-1} at 1 A g^{-1}, representing a 5-fold improvement over rGO SSC (Figure 5F). This value is greater

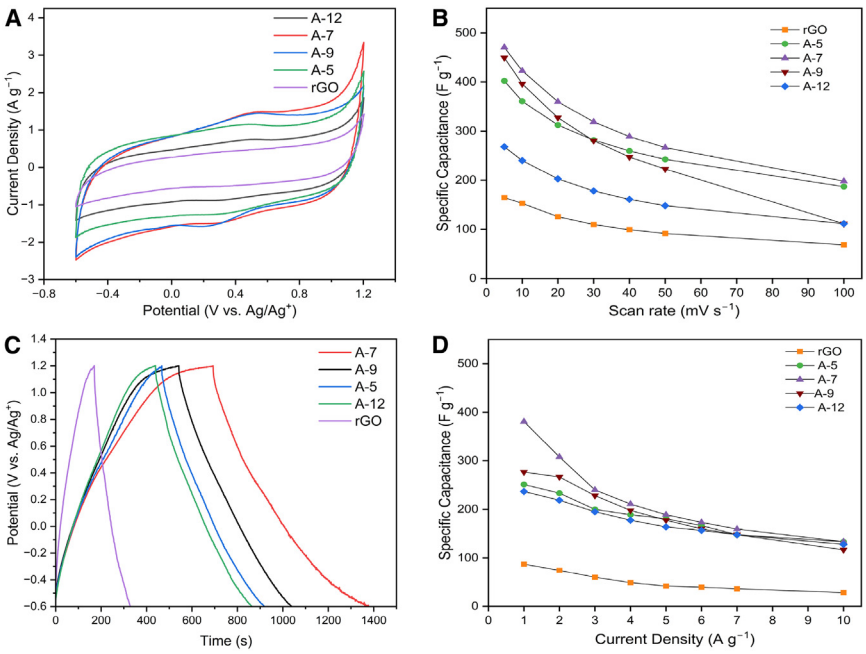

Figure 4. Electrochemical properties of NH_2−rGO and rGO in 1 M $EMIMBF_4$ electrolyte in three-electrode configuration

(A) CV curves at 5 mV s^{-1}.

(B) Variation of C_S with scan rate.

(C) GCD curves at 1 A g^{-1}.

(D) Variation of C_S with current density.

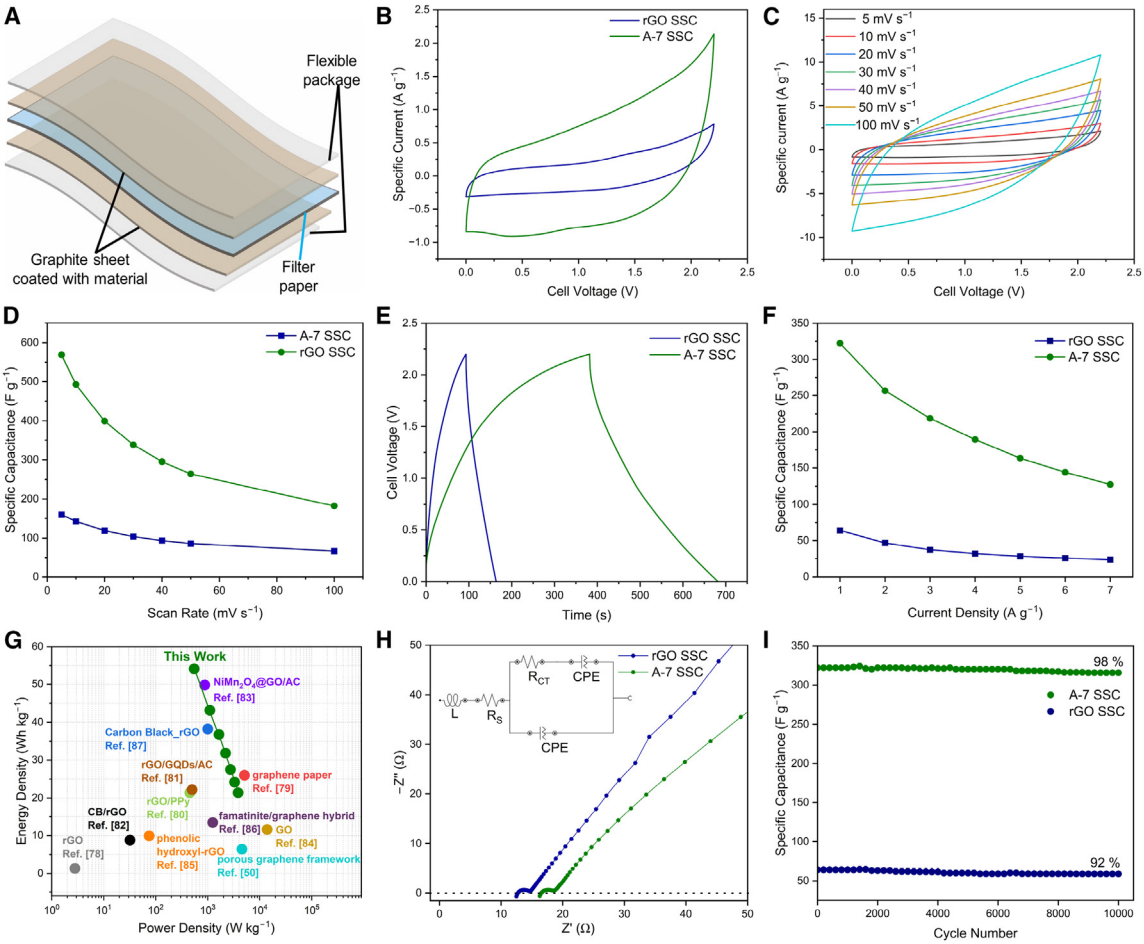

Figure 5. Schematic representation and electrochemical performance of the symmetric supercapacitors

(A) Schematic illustration of fabrication of symmetric supercapacitor device.

(B) CV curves at a scan rate of 5 mV s^{-1}.

(C) CV curves of A-7 SSC at different scan rates.

(D) C_S of the devices at different scan rates.

(E) GCD curves of the devices at 1 A g^{-1}.

(F) C_S of the devices at different current densities.

(G) Ragone plot.

(H) Nyquist plots of A-7 SSC and rGO SSC (inset is the circuits used for fitting of EIS curves).

(I) Cycling stability of A-7 SSC and rGO SSC at 7 A g^{-1}.

than those of N-doped graphene (205.3 F g^{-1} at 1 A g^{-1}), rGO (133 F g^{-1} at 1 A g^{-1}),[28] N-modified few-layer graphene (227 F g^{-1} at 1 A g^{-1}),[30] flame-induced rGO (260 F g^{-1} at 0.1 A g^{-1}),[56] porous graphene framework (237 F g^{-1} at 0.2 A g^{-1}),[50] holey graphene framework (298 F g^{-1} at 1 A g^{-1})[57] and is among the highest reported for supercapacitors based on graphene (Table 3). Additionally, A-7 SSC demonstrated its superiority in both gravimetric and volumetric terms. These metrics are critical in the portable energy storage market, where the simultaneous optimization of energy and power density is highly valued.[58–61] Energy density determines the overall energy storage capacity, while high power density allows for rapid charging/discharging. Although supercapacitors excel in providing high power densities, their energy density remains a significant limitation that needs improvement. A-7 SSC displayed an impressive gravimetric energy density of 54.18 Wh kg^{-1} at 1 A g^{-1}, five times higher than rGO SSC (10.77 Wh kg^{-1} at 1 A g^{-1}). A-7 SSC also demonstrated a volumetric energy density of 48.16 Wh L^{-1} at 1 A g^{-1} which is almost seven times greater as compared to rGO SSC (6.89 Wh L^{-1}). Moreover, at a current density of 7 A g^{-1}, the gravimetric and volumetric energy densities for A-7 SSC remained high at 21.39 Wh kg^{-1} and 19.01 Wh L^{-1}, while the volumetric and gravimetric power densities increased to 3422.22 Wh L^{-1} and 3850 Wh kg^{-1} respectively indicating much-enhanced performance. The Ragone plot in Figure 5G shows that the A-7 SSC outperforms many graphene-based supercapacitors, even exceeding some binary composites.[50,62–71]

Electrochemical impedance spectroscopy (EIS) tests were also performed to gain deeper insights into the capacitive

Table 3. Comparison of specific capacitance of carbon-based materials as supercapacitor electrodes

Materials	Gravimetric capacitance (F g^{-1})	Current density/ Scan rate	Electrolyte	Reference
High density porous graphene macroform	238	0.1 A g^{-1}	6 M KOH	Tao et al.[72]
S-porous carbon/graphene	109	0.05 A g^{-1}	6 M KOH	Seredych and Bandosz[73]
High density rGO	182	1 A g^{-1}	6 M KOH	Li and Zhao[74]
KOH activated graphene	165	1.4 A g^{-1}	BMIM BF_4/AN	Zhu et al.[75]
Activated microwave-expanded G-O spheres	174	4.2 A g^{-1}	[BMIM][BF_4]/AN	Kim et al.[76]
Holey graphene framework	298	1 A g^{-1}	EMIMBF_4/AN	Xu et al.[57]
Nitrogen-enriched nonporous carbon	115	0.05 A g^{-1}	1 M H_2SO_4	Hulicova-Jurcakova et al.[77]
Seaweed biopolymer-derived carbon	198	2 mV s^{-1}	1 M H_2SO_4	Raymundo-Piñero et al.[78]
Copper nanocrystal-modified activated carbon	79	0.2 A g^{-1}	TEATFB	Zhang et al.[79]
rGO	255	0.5 A g^{-1}	6 M KOH	Lei et al.[80]
3D nitrogen and boron co-doped graphene	239	1 A g^{-1}	1 M H_2SO_4	Wu et al.[81]
3D N-doped graphene-CNT	180	0.5 A g^{-1}	6 M KOH	You et al.[82]
B-doped graphene nanoplatelets	160	1 A g^{-1}	6 M KOH	Han et al.[83]
N-doped graphene sponge	286.86	5 mV s^{-1}	1 M NaCl	Xu et al.[84]
3D porous carbon	226	1 mV s^{-1}	1 M H_2SO_4	Wu et al.[85]
Graphene-cellulose paper	120	1 mV s^{-1}	1 M H_2SO_4	Weng et al.[86]
Graphene/Polyaniline composite paper	233	–	1 M H_2SO_4	Wang et al.[87]
NH_2-rGO	322	1 A g^{-1}	1 M EMIMBF_4/ACN	Present work

behavior of the devices. Figure 5H present the Nyquist plot comparisons for the devices. At high frequencies, the impedance data shifted from positive to negative, indicating inductive behavior in this region. This inductance is not related to the electrochemical processes within the supercapacitor but is instead attributed to stray inductance, commonly observed in supercapacitors and battery cells, and is primarily caused by cables and cell connections.[88] It is however important to account for this inductance during the fitting and simulation of experimental impedance data to determine the cell's electrical parameters accurately. The Nyquist plots also revealed a Warburg region and a smaller semicircle, indicating lower charge transfer resistance at the interfaces and the bulk material, which implies efficient electrolyte ion diffusion.[89,90] The plots were fitted utilizing an equivalent circuit (inset of Figure 5H), which revealed the equivalent series resistance to be ~12.7 Ω for rGO SSC and 15.5 Ω for A-7 SSC. Additionally, the charge transfer resistance was found to be low, at 2.05 Ω for rGO SSC and 2.03 Ω for A-7 SSC. The nearly vertical slope in the low-frequency region indicates highly capacitive behavior, which is in agreement with CV and GCD analysis.

Cycling stability is another crucial factor for practical applications. Figure 5I illustrates the cycling stability of A-7 SSC and rGO SSC, determined through a GCD test at 7 A g^{-1}. A-7 SSC shows a 98% capacitance retention after 10,000 cycles, compared to 92% for rGO SSC, indicating its excellent cyclability. For comparison, the reported capacitance retention of some high-performance graphene-based electrodes is 96.5% after 10,000 cycles for laser-scribed graphene capacitors,[91] 57% for capillary-densified graphene,[92] 97% for porous graphene frameworks,[50] 77% for polyoxometalate/rGO,[93] 79% for graphene/polyaniline nanofiber,[94] 90.3% for N-doped graphene,[29] and <90% for thermal reduced GO.[95] These comparisons underscore the exceptional charge transport capabilities of NH_2−rGO and its promising potential for use as supercapacitor electrodes.

Conclusion

In conclusion, we have demonstrated a simple and scalable method for synthesizing aminated reduced graphene oxide in a single step. This is currently one of the fastest synthesis methods available for this material, with the entire process completed in approximately 9 h. The nitrogen content can be adjusted by varying the pH of the reaction mixture, with ammonia serving as the nitrogen source. XPS and FTIR analyses validate the presence of primary amines in graphene. This method facilitates the reduction of graphene and the introduction of up to 6 atomic % of amines, with the XPS data indicating a minimal presence of other nitrogen species, such as pyridines. Elemental mapping reveals a uniform distribution of nitrogen throughout the NH_2−rGO matrix. The NH_2−rGO exhibited enhanced electrochemical performance compared to rGO, including a high specific capacitance in three-electrode configuration and symmetric supercapacitor devices. Specifically, A-7 SSC achieved the highest C_S of 322 F g^{-1} at a current density of 1 A g^{-1}, which is a 5-fold increase compared to rGO SSC.

Additionally, A-7 SSC demonstrated an impressive gravimetric energy density of 54.18 Wh kg^{-1} at 1 A g^{-1}, five times greater than rGO SSC (10.77 Wh kg^{-1} at 1 A g^{-1}) and a volumetric energy density of 48.16 Wh L^{-1} at 1 A g^{-1}, nearly seven

times higher than rGO SSC (6.89 Wh L^{-1}). The enhanced electrochemical performance of NH_2−rGO is attributed to improved wettability due to the introduction of nitrogen groups. This method provides a promising strategy for developing advanced high-performance energy storage systems based on graphene. Moreover, this approach could be adapted for post-synthesis modifications or activation of carbon nanomaterials, offering significant potential in catalysis, biosensors, and energy storage applications.

Limitations of the study

Due to equipment limitations, we were unable to perform additional materials characterization, including Raman spectroscopy, high-resolution transmission electron microscopy (HRTEM), and atomic force microscopy (AFM).

RESOURCE AVAILABILITY

Lead contact

Further information and requests for resources and reagents should be directed to and will be fulfilled by the lead contact, Dipak Sinha (dipaksinha@gmail.com).

Materials availability

The material produced in this study was aminated reduced graphene oxide, which was synthesized in our laboratory following the procedure outlined in the synthesis of NH_2−rGO section of the STAR Methods. The readers can purchase the chemicals to synthesize the materials, as described in the manuscript.

Data and code availability

- All data generated and/or analyzed during this study are included in the article and supplementary figures and tables.
- This paper does not report original code.
- Any additional information required to reanalyze the data reported in this article is available from the lead contact upon request.

ACKNOWLEDGEMENTS

The authors S.K. and P.B. acknowledge the financial assistance from the Department of Science and Technology, Ministry of Science and Technology, Government of India in the form of INSPIRE Fellowship (IF230103 and IF190895).

AUTHOR CONTRIBUTIONS

S.K., conceptualization, data curation, formal analysis, investigation, methodology, and writing– original draft; P.B., formal analysis, investigation, methodology, and writing - review and editing; K.R., writing - review and editing; N.R.M., writing - review and editing; D.R., supervision and writing - review and editing; D.S., supervision and writing - review and editing.

DECLARATION OF INTERESTS

An Indian patent with the application number 202431046163 A has been published.

STAR★METHODS

Detailed methods are provided in the online version of this paper and include the following:

- KEY RESOURCES TABLE
- EXPERIMENTAL MODEL AND STUDY PARTICIPANT DETAILS
- METHOD DETAILS
  - Synthesis of NH_2−rGO
  - Materials characterization
  - Electrochemical studies
- QUANTIFICATION AND STATISTICAL ANALYSIS

SUPPLEMENTAL INFORMATION

Supplemental information can be found online at https://doi.org/10.1016/j.isci.2025.112271.

Received: October 17, 2024
Revised: January 3, 2025
Accepted: March 18, 2025
Published: March 22, 2025

REFERENCES

1. Jha, P.K., Singh, S.K., Kumar, V., Rana, S., Kurungot, S., and Ballav, N. (2017). High-Level Supercapacitive Performance of Chemically Reduced Graphene Oxide. Chem *3*, 846–860. https://doi.org/10.1016/j.chempr.2017.08.011.
2. Kumar, S., Bora, P., Bhomick, P.C., Rangappa, D., and Sinha, D. (2025). Graphene-MXene van der Waals heterostructures for highperformance supercapacitors. Nano Research Energy *4*, e9120148. https://doi.org/10.26599/NRE.2024.9120148.
3. Wang, Y., and Wang, Y. (2023). Recent progress in MXene layers materials for supercapacitors: High-performance electrodes. SmartMat *4*, e1130. https://doi.org/10.1002/smm2.1130.
4. Liu, C., Yu, Z., Neff, D., Zhamu, A., and Jang, B.Z. (2010). Graphene-Based Supercapacitor with an Ultrahigh Energy Density. Nano Lett. *10*, 4863–4868. https://doi.org/10.1021/nl102661q.
5. Geim, A.K., and Novoselov, K.S. (2007). The rise of graphene. Nat. Mater. *6*, 183–191. https://doi.org/10.1038/nmat1849.
6. Kumar, S., Sharma, S., Karmaker, R., and Sinha, D. (2021). DFT study on the structural, optical and electronic properties of platinum group doped graphene. Mater. Today Commun. *26*, 101755. https://doi.org/10.1016/j.mtcomm.2020.101755.
7. Sun, X., Liu, Z., Welsher, K., Robinson, J.T., Goodwin, A., Zaric, S., and Dai, H. (2008). Nano-graphene oxide for cellular imaging and drug delivery. Nano Res. *1*, 203–212. https://doi.org/10.1007/s12274-008-8021-8.
8. Pumera, M., Ambrosi, A., Bonanni, A., Chng, E.L.K., and Poh, H.L. (2010). Graphene for Electrochemical Sensing and Biosensing. Trends Anal. Chem. *29*, 954–965. https://doi.org/10.1016/j.trac.2010.05.011.
9. Blake, P., Brimicombe, P.D., Nair, R.R., Booth, T.J., Jiang, D., Schedin, F., Ponomarenko, L.A., Morozov, S.V., Gleeson, H.F., Hill, E.W., et al. (2008). Graphene-Based Liquid Crystal Device. Nano Lett. *8*, 1704–1708. https://doi.org/10.1021/nl080649i.
10. Wang, B., Ruan, T., Chen, Y., Jin, F., Peng, L., Zhou, Y., Wang, D., and Dou, S. (2020). Graphene-based composites for electrochemical energy storage. Energy Storage Mater. *24*, 22–51. https://doi.org/10.1016/j.ensm.2019.08.004.
11. Chakraborty, S., Saha, S., Dhanak, V.R., Biswas, K., Barbezat, M., Terrasi, G.P., and Chakraborty, A.K. (2016). High yield synthesis of amine functionalized graphene oxide and its surface properties. RSC Adv. *6*, 67916–67924. https://doi.org/10.1039/C6RA12844K.
12. Lai, L., Chen, L., Zhan, D., Sun, L., Liu, J., Lim, S.H., Poh, C.K., Shen, Z., and Lin, J. (2011). One-step synthesis of NH_2-graphene from in situ graphene-oxide reduction and its improved electrochemical properties. Carbon N. Y. *49*, 3250–3257. https://doi.org/10.1016/j.carbon.2011.03.051.
13. Paton, K.R., Varrla, E., Backes, C., Smith, R.J., Khan, U., O'Neill, A., Boland, C., Lotya, M., Istrate, O.M., King, P., et al. (2014). Scalable production of large quantities of defect-free few-layer graphene by shear

exfoliation in liquids. Nat. Mater. *13*, 624–630. https://doi.org/10.1038/nmat3944.

14. Marcano, D.C., Kosynkin, D.V., Berlin, J.M., Sinitskii, A., Sun, Z., Slesarev, A., Alemany, L.B., Lu, W., and Tour, J.M. (2010). Improved Synthesis of Graphene Oxide. ACS Nano *4*, 4806–4814. https://doi.org/10.1021/nn1006368.
15. Stankovich, S., Piner, R.D., Nguyen, S.T., and Ruoff, R.S. (2006). Synthesis and exfoliation of isocyanate-treated graphene oxide nanoplatelets. Carbon N. Y. *44*, 3342–3347. https://doi.org/10.1016/j.carbon.2006.06.004.
16. Chen, Y., Zhang, X., Zhang, D., Yu, P., and Ma, Y. (2011). High performance supercapacitors based on reduced graphene oxide in aqueous and ionic liquid electrolytes. Carbon N. Y. *49*, 573–580. https://doi.org/10.1016/j.carbon.2010.09.060.
17. Wu, Z.-S., Ren, W., Gao, L., Zhao, J., Chen, Z., Liu, B., Tang, D., Yu, B., Jiang, C., and Cheng, H.-M. (2009). Synthesis of Graphene Sheets with High Electrical Conductivity and Good Thermal Stability by Hydrogen Arc Discharge Exfoliation. ACS Nano *3*, 411–417. https://doi.org/10.1021/nn900020u.
18. Bakandritsos, A., Jakubec, P., Pykal, M., and Otyepka, M. (2019). Covalently functionalized graphene as a supercapacitor electrode material. FlatChem *13*, 25–33. https://doi.org/10.1016/j.flatc.2018.12.004.
19. Zhuo, Y., Prestat, E., Kinloch, I.A., and Bissett, M.A. (2022). Self-Assembled 1T-MoS_2/Functionalized Graphene Composite Electrodes for Supercapacitor Devices. ACS Appl. Energy Mater. *5*, 61–70. https://doi.org/10.1021/acsaem.1c02203.
20. Andooz, A., Kowsari, E., Najafi, M.D., Chinnappan, A., Eshlaghi, M.A., and Ramakrishna, S. (2024). Zolmitriptan-functionalized graphene oxide and its composite with [Bmim] [$FeCl_4$] ionic liquid and biochar derived from the pyrolysis of Heracleum Persicum for supercapacitor application. Electrochim. Acta *477*, 143773. https://doi.org/10.1016/j.electacta.2024.143773.
21. Zhou, T., Wu, C., Wang, Y., Tomsia, A.P., Li, M., Saiz, E., Fang, S., Baughman, R.H., Jiang, L., and Cheng, Q. (2020). Super-tough MXene-functionalized graphene sheets. Nat. Commun. *11*, 2077. https://doi.org/10.1038/s41467-020-15991-6.
22. Kuila, T., Bose, S., Mishra, A.K., Khanra, P., Kim, N.H., and Lee, J.H. (2012). Chemical functionalization of graphene and its applications. Prog. Mater. Sci. *57*, 1061–1105. https://doi.org/10.1016/j.pmatsci.2012.03.002.
23. Rabchinskii, M.K., Shnitov, V.V., Dideikin, A.T., Aleksenskii, A.E., Vul', S.P., Baidakova, M.V., Pronin, I.I., Kirilenko, D.A., Brunkov, P.N., Weise, J., and Molodtsov, S.L. (2016). Nanoscale Perforation of Graphene Oxide during Photoreduction Process in the Argon Atmosphere. J. Phys. Chem. C *120*, 28261–28269. https://doi.org/10.1021/acs.jpcc.6b08758.
24. Baraket, M., Stine, R., Lee, W.K., Robinson, J.T., Tamanaha, C.R., Sheehan, P.E., and Walton, S.G. (2012). Aminated graphene for DNA attachment produced via plasma functionalization. Appl. Phys. Lett. *100*, 233123. https://doi.org/10.1063/1.4711771.
25. Kang, M.A., Ji, S., Kim, S., Park, C.Y., Myung, S., Song, W., Lee, S.S., Lim, J., and An, K.S. (2018). Highly sensitive and wearable gas sensors consisting of chemically functionalized graphene oxide assembled on cotton yarn. RSC Adv. *8*, 11991–11996. https://doi.org/10.1039/C8RA01184B.
26. Suvarnaphaet, P., and Pechprasarn, S. (2017). Graphene-Based Materials for Biosensors: A Review. Sensors *17*, 2161. https://doi.org/10.3390/s17102161.
27. Hernandez, Y., Nicolosi, V., Lotya, M., Blighe, F.M., Sun, Z., De, S., McGovern, I.T., Holland, B., Byrne, M., Gun'Ko, Y.K., et al. (2008). High-yield production of graphene by liquid-phase exfoliation of graphite. Nat. Nanotechnol. *3*, 563–568. https://doi.org/10.1038/nnano.2008.215.
28. Liu, Y.Z., Li, Y.F., Su, F.Y., Xie, L.J., Kong, Q.Q., Li, X.M., Gao, J.G., and Chen, C.-M. (2016). Easy one-step synthesis of N-doped graphene for supercapacitors. Energy Storage Mater. *2*, 69–75. https://doi.org/10.1016/j.ensm.2015.09.006.
29. Haque, E., Islam, M.M., Pourazadi, E., Hassan, M., Faisal, S.N., Roy, A.K., Konstantinov, K., Harris, A.T., Minett, A.I., and Gomes, V.G. (2015). Nitrogen doped graphene via thermal treatment of composite solid precursors as a high performance supercapacitor. RSC Adv. *5*, 30679–30686. https://doi.org/10.1039/C4RA17262K.
30. Šedajová, V., Bakandritsos, A., Błoński, P., Medveď, M., Langer, R., Zaoralová, D., Ugolotti, J., Dzíbelová, J., Jakubec, P., Kupka, V., and Otyepka, M. (2022). Nitrogen doped graphene with diamond-like bonds achieves unprecedented energy density at high power in a symmetric sustainable supercapacitor. Energy Environ. Sci. *15*, 740–748. https://doi.org/10.1039/D1EE02234B.
31. Lota, G., Grzyb, B., Machnikowska, H., Machnikowski, J., and Frackowiak, E. (2005). Effect of nitrogen in carbon electrode on the supercapacitor performance. Chem. Phys. Lett. *404*, 53–58. https://doi.org/10.1016/j.cplett.2005.01.074.
32. Rabchinskii, M.K., Ryzhkov, S.A., Kirilenko, D.A., Ulin, N.V., Baidakova, M.V., Shnitov, V.V., Pavlov, S.I., Chumakov, R.G., Stolyarova, D.Y., Besedina, N.A., et al. (2020). From graphene oxide towards aminated graphene: facile synthesis, its structure and electronic properties. Sci. Rep. *10*, 6902. https://doi.org/10.1038/s41598-020-63935-3.
33. Semenov, K.N., Andrusenko, E.V., Charykov, N.A., Litasova, E.V., Panova, G.G., Penkova, A.V., Murin, I.V., and Piotrovskiy, L.B. (2017). Carboxylated fullerenes: Physico-chemical properties and potential applications. Prog. Solid State Chem. *47–48*, 19–36. https://doi.org/10.1016/j.progsolidstchem.2017.09.001.
34. Marsden, A.J., Brommer, P., Mudd, J.J., Dyson, M.A., Cook, R., Asensio, M., Avila, J., Levy, A., Sloan, J., Quigley, D., et al. (2015). Effect of oxygen and nitrogen functionalization on the physical and electronic structure of graphene. Nano Res. *8*, 2620–2635. https://doi.org/10.1007/s12274-015-0768-0.
35. Krasteva, N., Keremidarska-Markova, M., Hristova-Panusheva, K., Andreeva, T., Speranza, G., Wang, D., Draganova-Filipova, M., Miloshev, G., and Georgieva, M. (2019). Aminated graphene oxide as a potential new therapy for colorectal cancer. Oxid. Med. Cell. Longev. *2019*, 3738980. https://doi.org/10.1155/2019/3738980.
36. Valentini, L., Cardinali, M., Bittolo Bon, S., Bagnis, D., Verdejo, R., Lopez-Manchado, M.A., and Kenny, J.M. (2010). Use of butylamine modified graphene sheets in polymer solar cells. J. Mater. Chem. *20*, 995–1000. https://doi.org/10.1039/B919327H.
37. Zhang, W., Ma, J., Gao, D., Zhou, Y., Li, C., Zha, J., and Zhang, J. (2016). Preparation of amino-functionalized graphene oxide by Hoffman rearrangement and its performances on polyacrylate coating latex. Prog. Org. Coat. *94*, 9–17. https://doi.org/10.1016/j.porgcoat.2016.01.013.
38. Papageorgiou, D.G., Kinloch, I.A., and Young, R.J. (2017). Mechanical properties of graphene and graphene-based nanocomposites. Prog. Mater. Sci. *90*, 75–127. https://doi.org/10.1016/j.pmatsci.2017.07.004.
39. Seredych, M., and Bandosz, T.J. (2007). Mechanism of Ammonia Retention on Graphite Oxides: Role of Surface Chemistry and Structure. J. Phys. Chem. C *111*, 15596–15604. https://doi.org/10.1021/jp0735785.
40. Stankovich, S., Dikin, D.A., Piner, R.D., Kohlhaas, K.A., Kleinhammes, A., Jia, Y., Wu, Y., Nguyen, S.T., and Ruoff, R.S. (2007). Synthesis of graphene-based nanosheets via chemical reduction of exfoliated graphite oxide. Carbon N. Y. *45*, 1558–1565. https://doi.org/10.1016/j.carbon.2007.02.034.
41. Fan, X., Peng, W., Li, Y., Li, X., Wang, S., Zhang, G., and Zhang, F. (2008). Deoxygenation of Exfoliated Graphite Oxide under Alkaline Conditions: A Green Route to Graphene Preparation. Adv. Mater. *20*, 4490–4493. https://doi.org/10.1002/adma.200801306.
42. Perera, S.D., Mariano, R.G., Nijem, N., Chabal, Y., Ferraris, J.P., and Balkus, K.J. (2012). Alkaline deoxygenated graphene oxide for supercapacitor applications: An effective green alternative for chemically reduced

graphene. J. Power Sources *215*, 1–10. https://doi.org/10.1016/j.jpowsour.2012.04.059.

43. Lai, L., Huang, G., Wang, X., and Weng, J. (2010). Solvothermal syntheses of hollow carbon microspheres modified with $-NH_2$ and –OH groups in one-step process. Carbon N. Y. *48*, 3145–3156. https://doi.org/10.1016/j.carbon.2010.04.053.
44. Gromov, A., Dittmer, S., Svensson, J., Nerushev, O.A., Perez-García, S.A., Licea-Jiménez, L., Rychwalski, R., and Campbell, E.E.B. (2005). Covalent amino-functionalisation of single-wall carbon nanotubes. J. Mater. Chem. *15*, 3334–3339. https://doi.org/10.1039/B504282H.
45. Caliman, C.C., Mesquita, A.F., Cipriano, D.F., Freitas, J.C.C., Cotta, A.A.C., Macedo, W.A.A., and Porto, A.O. (2018). One-pot synthesis of amine-functionalized graphene oxide by microwave-assisted reactions: an outstanding alternative for supporting materials in supercapacitors. RSC Adv. *8*, 6136–6145. https://doi.org/10.1039/C7RA13514A.
46. Si, Y., and Samulski, E.T. (2008). Synthesis of Water Soluble Graphene. Nano Lett. *8*, 1679–1682. https://doi.org/10.1021/nl080604h.
47. Wang, Y., Shi, Z., Huang, Y., Ma, Y., Wang, C., Chen, M., and Chen, Y. (2009). Supercapacitor Devices Based on Graphene Materials. J. Phys. Chem. C *113*, 13103–13107. https://doi.org/10.1021/jp902214f.
48. Stobinski, L., Lesiak, B., Malolepszy, A., Mazurkiewicz, M., Mierzwa, B., Zemek, J., Jiricek, P., and Bieloshapka, I. (2014). Graphene oxide and reduced graphene oxide studied by the XRD, TEM and electron spectroscopy methods. J. Electron Spectros. Relat. Phenomena *195*, 145–154. https://doi.org/10.1016/j.elspec.2014.07.003.
49. Jankovský, O., Šimek, P., Klimová, K., Sedmidubský, D., Matějková, S., Pumera, M., and Sofer, Z. (2014). Towards graphene bromide: bromination of graphite oxide. Nanoscale *6*, 6065–6074. https://doi.org/10.1039/C4NR01154F.
50. Yuan, K., Xu, Y., Uihlein, J., Brunklaus, G., Shi, L., Heiderhoff, R., Que, M., Forster, M., Chassé, T., Pichler, T., et al. (2015). Straightforward Generation of Pillared, Microporous Graphene Frameworks for Use in Supercapacitors. Adv. Mater. *27*, 6714–6721. https://doi.org/10.1002/adma.201503390.
51. Han, S., Wu, D., Li, S., Zhang, F., and Feng, X. (2014). Porous Graphene Materials for Advanced Electrochemical Energy Storage and Conversion Devices. Adv. Mater. *26*, 849–864. https://doi.org/10.1002/adma.201303115.
52. Aboutalebi, S.H., Chidembo, A.T., Salari, M., Konstantinov, K., Wexler, D., Liu, H.K., and Dou, S.X. (2011). Comparison of GO, GO/MWCNTs composite and MWCNTs as potential electrode materials for supercapacitors. Energy Environ. Sci. *4*, 1855–1865. https://doi.org/10.1039/C1EE01039E.
53. Aunkor, M.T.H., Mahbubul, I.M., Saidur, R., and Metselaar, H.S.C. (2016). The green reduction of graphene oxide. RSC Adv. *6*, 27807–27828. https://doi.org/10.1039/C6RA03189G.
54. Hulicova-Jurcakova, D., Seredych, M., Lu, G.Q., and Bandosz, T.J. (2009). Combined Effect of Nitrogen- and Oxygen-Containing Functional Groups of Microporous Activated Carbon on its Electrochemical Performance in Supercapacitors. Adv. Funct. Mater. *19*, 438–447. https://doi.org/10.1002/adfm.200801236.
55. Yu, D., Goh, K., Wang, H., Wei, L., Jiang, W., Zhang, Q., Dai, L., and Chen, Y. (2014). Scalable synthesis of hierarchically structured carbon nanotube–graphene fibres for capacitive energy storage. Nat. Nanotechnol. *9*, 555–562. https://doi.org/10.1038/nnano.2014.93.
56. Liu, Y.-Z., Chen, C.-M., Li, Y.-F., Li, X.-M., Kong, Q.-Q., and Wang, M.-Z. (2014). Crumpled reduced graphene oxide by flame-induced reduction of graphite oxide for supercapacitive energy storage. J. Mater. Chem. A *2*, 5730–5737. https://doi.org/10.1039/C3TA15082H.
57. Xu, Y., Lin, Z., Zhong, X., Huang, X., Weiss, N.O., Huang, Y., and Duan, X. (2014). Holey graphene frameworks for highly efficient capacitive energy storage. Nat. Commun. *5*, 4554. https://doi.org/10.1038/ncomms5554.
58. Gogotsi, Y., and Simon, P. (2011). True Performance Metrics in Electrochemical Energy Storage. Science *334*, 917–918. https://doi.org/10.1126/science.1213003.
59. Li, H., Tao, Y., Zheng, X., Luo, J., Kang, F., Cheng, H.-M., and Yang, Q.-H. (2016). Ultra-thick graphene bulk supercapacitor electrodes for compact energy storage. Energy Environ. Sci. *9*, 3135–3142. https://doi.org/10.1039/C6EE00941G.
60. Jin, H., Feng, X., Li, J., Li, M., Xia, Y., Yuan, Y., Yang, C., Dai, B., Lin, Z., Wang, J., et al. (2019). Heteroatom-Doped Porous Carbon Materials with Unprecedented High Volumetric Capacitive Performance. Angew. Chem. Int. Ed. Engl. *58*, 2397–2401. https://doi.org/10.1002/anie.201813686.
61. Li, Z., Gadipelli, S., Li, H., Howard, C.A., Brett, D.J.L., Shearing, P.R., Guo, Z., Parkin, I.P., and Li, F. (2020). Tuning the interlayer spacing of graphene laminate films for efficient pore utilization towards compact capacitive energy storage. Nat. Energy *5*, 160–168. https://doi.org/10.1038/s41560-020-0560-6.
62. Lei, Z., Christov, N., and Zhao, X.S. (2011). Intercalation of mesoporous carbon spheres between reduced graphene oxide sheets for preparing high-rate supercapacitor electrodes. Energy Environ. Sci. *4*, 1866–1873. https://doi.org/10.1039/C1EE01094H.
63. Wang, G., Sun, X., Lu, F., Sun, H., Yu, M., Jiang, W., Liu, C., and Lian, J. (2012). Flexible Pillared Graphene-Paper Electrodes for High-Performance Electrochemical Supercapacitors. Small *8*, 452–459. https://doi.org/10.1002/smll.201101719.
64. Fan, L.-Q., Liu, G.J., Wu, J.H., Liu, L., Lin, J.M., and Wei, Y.L. (2014). Asymmetric supercapacitor based on graphene oxide/polypyrrole composite and activated carbon electrodes. Electrochim. Acta *137*, 26–33. https://doi.org/10.1016/j.electacta.2014.05.137.
65. Hao, H., Wang, J., Lv, Q., Jiao, Y., Li, J., Li, W., Akpinar, I., Shen, W., and He, G. (2020). Interfacial engineering of reduced graphene oxide for high-performance supercapacitor materials. J. Electroanal. Chem. *878*, 114679. https://doi.org/10.1016/j.jelechem.2020.114679.
66. Rapisarda, M., Damasco, A., Abbate, G., and Meo, M. (2020). Carbon black and reduced graphene oxide nanocomposite for binder-free supercapacitors with reduced graphene oxide paper as the current collector. ACS Omega *5*, 32426–32435. https://doi.org/10.1021/acsomega.0c04530.
67. Kanagambal, P., Ahamed, A.J., Rajeswaran, P., and Kamatchi, T. (2023). Hybrids of porous $NiMn_2O_4$@reduced graphene oxide composites for asymmetric supercapacitor applications. J. Mater. Sci. Mater. Electron. *34*, 1873. https://doi.org/10.1007/s10854-023-11298-6.
68. Down, M.P., Rowley-Neale, S.J., Smith, G.C., and Banks, C.E. (2018). Fabrication of Graphene Oxide Supercapacitor Devices. ACS Appl. Energy Mater. *1*, 707–714. https://doi.org/10.1021/acsaem.7b00164.
69. Zhang, Y., Wen, G., Fan, S., Chu, Y., Li, S., Xu, B., and Zhang, J. (2019). Phenolic hydroxyl functionalized partially reduced graphene oxides for symmetric supercapacitors with significantly enhanced electrochemical performance. J. Power Sources *435*, 226799. https://doi.org/10.1016/j.jpowsour.2019.226799.
70. Mariappan, V.K., Krishnamoorthy, K., Pazhamalai, P., Sahoo, S., Kesavan, D., and Kim, S.-J. (2019). Two dimensional famatinite sheets decorated on reduced graphene oxide: A novel electrode for high performance supercapacitors. J. Power Sources *433*, 126648. https://doi.org/10.1016/j.jpowsour.2019.05.056.
71. Lv, H., Yuan, Y., Xu, Q., Liu, H., Wang, Y.-G., and Xia, Y. (2018). Carbon quantum dots anchoring MnO2/graphene aerogel exhibits excellent performance as electrode materials for supercapacitor. J. Power Sources *398*, 167–174. https://doi.org/10.1016/j.jpowsour.2018.07.059.
72. Tao, Y., Xie, X., Lv, W., Tang, D.-M., Kong, D., Huang, Z., Nishihara, H., Ishii, T., Li, B., Golberg, D., et al. (2013). Towards ultrahigh volumetric capacitance: graphene derived highly dense but porous carbons for supercapacitors. Sci. Rep. *3*, 2975. https://doi.org/10.1038/srep02975.
73. Seredych, M., and Bandosz, T.J. (2013). S-doped micro/mesoporous carbon–graphene composites as efficient supercapacitors in alkaline media. J. Mater. Chem. A Mater. *1*, 11717–11727. https://doi.org/10.1039/C3TA12252B.

74. Li, Y., and Zhao, D. (2015). Preparation of reduced graphite oxide with high volumetric capacitance in supercapacitors. Chem. Commun. *51*, 5598–5601. https://doi.org/10.1039/C4CC08038F.

75. Zhu, Y., Murali, S., Stoller, M.D., Ganesh, K.J., Cai, W., Ferreira, P.J., Pirkle, A., Wallace, R.M., Cychosz, K.A., Thommes, M., et al. (2011). Carbon-Based Supercapacitors Produced by Activation of Graphene. Science *332*, 1537–1541. https://doi.org/10.1126/science.1200770.

76. Kim, T., Jung, G., Yoo, S., Suh, K.S., and Ruoff, R.S. (2013). Activated Graphene-Based Carbons as Supercapacitor Electrodes with Macro- and Mesopores. ACS Nano *7*, 6899–6905. https://doi.org/10.1021/nn402077v.

77. Hulicova-Jurcakova, D., Kodama, M., Shiraishi, S., Hatori, H., Zhu, Z.H., and Lu, G.Q. (2009). Nitrogen-Enriched Nonporous Carbon Electrodes with Extraordinary Supercapacitance. Adv. Funct. Mater. *19*, 1800–1809. https://doi.org/10.1002/adfm.200801100.

78. Raymundo-Piñero, E., Leroux, F., and Béguin, F. (2006). A High-Performance Carbon for Supercapacitors Obtained by Carbonization of a Seaweed Biopolymer. Adv. Mater. *18*, 1877–1882. https://doi.org/10.1002/adma.200501905.

79. Zhang, L., Candelaria, S.L., Tian, J., Li, Y., Huang, Y.x., and Cao, G. (2013). Copper nanocrystal modified activated carbon for supercapacitors with enhanced volumetric energy and power density. J. Power Sources *236*, 215–223. https://doi.org/10.1016/j.jpowsour.2013.02.036.

80. Lei, Z., Lu, L., and Zhao, X.S. (2012). The electrocapacitive properties of graphene oxide reduced by urea. Energy Environ. Sci. *5*, 6391–6399. https://doi.org/10.1039/C1EE02478G.

81. Wu, Z.-S., Winter, A., Chen, L., Sun, Y., Turchanin, A., Feng, X., and Müllen, K. (2012). Three-Dimensional Nitrogen and Boron Co-doped Graphene for High-Performance All-Solid-State Supercapacitors. Adv. Mater. *24*, 5130–5135. https://doi.org/10.1002/adma.201201948.

82. You, B., Wang, L., Yao, L., and Yang, J. (2013). Three dimensional N-doped graphene–CNT networks for supercapacitor. Chem. Commun. *49*, 5016–5018. https://doi.org/10.1039/C3CC41949E.

83. Han, J., Zhang, L.L., Lee, S., Oh, J., Lee, K.-S., Potts, J.R., Ji, J., Zhao, X., Ruoff, R.S., and Park, S. (2013). Generation of B-Doped Graphene Nanoplatelets Using a Solution Process and Their Supercapacitor Applications. ACS Nano *7*, 19–26. https://doi.org/10.1021/nn3034309.

84. Xu, X., Sun, Z., Chua, D.H.C., and Pan, L. (2015). Novel nitrogen doped graphene sponge with ultrahigh capacitive deionization performance. Sci. Rep. *5*, 11225. https://doi.org/10.1038/srep11225.

85. Wu, Z.S., Sun, Y., Tan, Y.-Z., Yang, S., Feng, X., and Müllen, K. (2012). Three-Dimensional Graphene-Based Macro- and Mesoporous Frameworks for High-Performance Electrochemical Capacitive Energy Storage. J. Am. Chem. Soc. *134*, 19532–19535. https://doi.org/10.1021/ja308676h.

86. Weng, Z., Su, Y., Wang, D.W., Li, F., Du, J., and Cheng, H.M. (2011). Graphene–Cellulose Paper Flexible Supercapacitors. Adv. Energy Mater. *1*, 917–922. https://doi.org/10.1002/aenm.201100312.

87. Wang, D.-W., Li, F., Zhao, J., Ren, W., Chen, Z.-G., Tan, J., Wu, Z.-S., Gentle, I., Lu, G.Q., and Cheng, H.-M. (2009). Fabrication of Graphene/Polyaniline Composite Paper via In Situ Anodic Electropolymerization for High-Performance Flexible Electrode. ACS Nano *3*, 1745–1752. https://doi.org/10.1021/nn900297m.

88. Sopčić, S., Antonić, D., and Mandić, Z. (2022). Effects of the composition of active carbon electrodes on the impedance performance of the AC/AC supercapacitors. J. Solid State Electrochem. *26*, 591–605. https://doi.org/10.1007/s10008-021-05112-8.

89. Wang, J., Tang, J., Ding, B., Malgras, V., Chang, Z., Hao, X., Wang, Y., Dou, H., Zhang, X., and Yamauchi, Y. (2017). Hierarchical porous carbons with layer-by-layer motif architectures from confined soft-template self-assembly in layered materials. Nat. Commun. *8*, 15717. https://doi.org/10.1038/ncomms15717.

90. Lei, Y., Li, Y., Chen, Y.Z., Xie, Y.W., Chen, Y.S., Wang, S.H., Wang, J., Shen, B.G., Pryds, N., Hwang, H.Y., and Sun, J.R. (2014). Visible-light-enhanced gating effect at the LaAlO3/SrTiO3 interface. Nat. Commun. *5*, 5554. https://doi.org/10.1038/ncomms6554.

91. El-Kady, M.F., and Kaner, R.B. (2013). Scalable fabrication of high-power graphene micro-supercapacitors for flexible and on-chip energy storage. Nat. Commun. *4*, 1475. https://doi.org/10.1038/ncomms2446.

92. Li, P., Li, H., Han, D., Shang, T., Deng, Y., Tao, Y., Lv, W., and Yang, Q.-H. (2019). Packing Activated Carbons into Dense Graphene Network by Capillarity for High Volumetric Performance Supercapacitors. Adv. Sci. *6*, 1802355. https://doi.org/10.1002/advs.201802355.

93. Yang, M., Choi, B.G., Jung, S.C., Han, Y.-K., Huh, Y.S., and Lee, S.B. (2014). Polyoxometalate-coupled Graphene via Polymeric Ionic Liquid Linker for Supercapacitors. Adv. Funct. Mater. *24*, 7301–7309. https://doi.org/10.1002/adfm.201401798.

94. Wu, Q., Xu, Y., Yao, Z., Liu, A., and Shi, G. (2010). Supercapacitors Based on Flexible Graphene/Polyaniline Nanofiber Composite Films. ACS Nano *4*, 1963–1970. https://doi.org/10.1021/nn1000035.

95. Ji, L., Meduri, P., Agubra, V., Xiao, X., and Alcoutlabi, M. (2016). Graphene-Based Nanocomposites for Energy Storage. Adv. Energy Mater. *6*, 1502159. https://doi.org/10.1002/aenm.201502159.

96. Hummers, W.S., Jr., and Offeman, R.E. (1958). Preparation of Graphitic Oxide. J. Am. Chem. Soc. *80*, 1339. https://doi.org/10.1021/ja01539a017.

97. Sethi, M., Shenoy, U.S., and Bhat, D.K. (2020). A porous graphene–Ni-Fe_2O_4 nanocomposite with high electrochemical performance and high cycling stability for energy storage applications. Nanoscale Adv. *2*, 4229–4241. https://doi.org/10.1039/D0NA00440E.

98. Xiang, C., Li, M., Zhi, M., Manivannan, A., and Wu, N. (2013). A reduced graphene oxide/Co3O4 composite for supercapacitor electrode. J. Power Sources *226*, 65–70. https://doi.org/10.1016/j.jpowsour.2012.10.064.

STAR★METHODS

KEY RESOURCES TABLE

REAGENT or RESOURCE	SOURCE	IDENTIFIER
Chemicals, peptides, and recombinant proteins		
Graphite Powder	Sigma Aldrich	7782-42-5
Sulfuric acid (~98%)	Sigma Aldrich	7664-93-9
Potassium permanganate	Sigma Aldrich	7722-64-7
Ethanol	Sigma Aldrich	64-17-5
Ammonia solution extrapure AR, 30%	Sisco Research Laboratories Pvt. Ltd., India	1336-21-6
De-ionized water	Milli-Q	Resistivity 18.2 MΩ cm @ 25°C
L-Ascorbic acid AR, 99.7%	Sisco Research Laboratories Pvt. Ltd., India	50-81-7
Sodium Hydroxide Pellets ACS, 97%	Sisco Research Laboratories Pvt. Ltd., India	1310-73-2
1-Ethyl-3-Methylimidazolium Tetrafluoroborate (EMIM BF_4) extrapure, 97%	Sisco Research Laboratories Pvt. Ltd., India	143314-16-3
Acetonitrile (ACN) ACS, 99.5%	Sisco Research Laboratories Pvt. Ltd., India	75-05-8
Poly(vinylidene fluoride) (average M_w ~534,000 by GPC, powder)	Sigma Aldrich	24937-79-9
N-Methyl-2-Pyrrolidone (NMP) extrapure AR, 99.5%	Sisco Research Laboratories Pvt. Ltd., India	872-50-4
Software and algorithms		
ImageJ	https://imagej.net/ij/index.html	https://www.nature.com/articles/nmeth.2089
OriginLab	https://www.originlab.com/	OriginPro 2024b (Learning Edition)
Other		
Autolab PGSTAT204 Electrochemical workstation	Metrohm	https://www.metrohm.com/en_in/products/a/ut20/aut204_s.html

EXPERIMENTAL MODEL AND STUDY PARTICIPANT DETAILS

There are no experimental models (animals, human subjects, plants, microbe strains, cell lines, primary cell cultures) used in the study.

METHOD DETAILS

Synthesis of NH_2−rGO

NH_2−rGO was synthesized using modified Hummer's method with some significant modifications.[96] In brief, 23 mL of concentrated H_2SO_4 was added to 1 g of graphite powder, and the RM was placed in an ice bath to maintain a low temperature. $NaNO_3$ was not used in this synthesis because it emits toxic gases, which may be detrimental to large-scale production. Later, 6g $KMnO_4$ was slowly introduced in small proportions to the RM, ensuring that the temperature remained <10°C with continuous stirring. Next, the RM was stirred at 35°C for 30 min, and then 70 mL of de-ionized H_2O was added. The RM was further subjected to sonication for 30 min and was stirred for another 30 min. At this stage, ammonia solution was added to the RM to adjust the pH, a crucial step that allows precise control over the concentration of nitrogen species incorporated into graphene. The pH was carefully controlled and set to specific values of 5, 7, 9, and 12, producing four distinct samples named A-5, A-7, A-9, and A-12, respectively. Subsequently, 100 mL of 1M L-ascorbic acid was introduced to the RM, and the mixture was refluxed at 95°C for 1 h to facilitate the reduction process. The reaction product was thoroughly washed with deionized water until the pH of the solution reached ~7 to remove any residual impurities. The resulting blackish powder solid was dried at 50°C to produce NH_2−rGO.

In order to make a comparison, we synthesized reduced graphene oxide using the same process except in this case, we used NaOH to adjust the pH to ~7 and was washed with 5% HCl and DI H_2O. The other experimental conditions are the same. The prepared materials were subsequently characterized using a range of analytical techniques.

Materials characterization

Powder X-ray diffraction was recorded using a Philips X'pert Pro X-ray diffractometer with Cu Kα radiation (k = 1.54056 Å). Scanning electron microscope images were obtained with field-emission scanning electron microscope (JSM 7900F, JEOL). Infrared transmission spectra were recorded with a PerkinElmer Spectrum Two Fourier transform infrared spectrometer with ATR in the 450-4000 cm^{-1} range with a resolution of 1 cm^{-1}. X-ray photoelectron spectroscopy measurements were made using Thermofisher Nexsa system employing an Al Kα X-ray source (1486.6 eV).

Electrochemical studies

All electrochemical measurements were performed on an Autolab PGSTAT204 electrochemical workstation (Metrohm, The Netherlands) with 1 M $EMIMBF_4$ in acetonitrile as the electrolyte. Both three-electrode and two-electrode configurations were used to evaluate the electrochemical performance. In the three-electrode setup, a platinum mesh (area = 1 cm × 1 cm) served as the counter electrode, and a Ag/Ag^+ non-aqueous electrode filled with a 2 M LiCl solution in ethanol was used as the reference electrode. The working electrodes were prepared by blending the active material, poly(vinylidene fluoride) (PVDF) and carbon black in a ratio of 85:10:5 in a mortar with NMP solvent, and then ground with a pestle. The resulting slurry was coated onto a graphite sheet (1 cm × 1 cm) and vacuum dried at 70°C for 16 h. The three-electrode measurements were conducted at room temperature (27°C ± 3).

CV and GCD were carried out at different scan rates and current densities across a potential window of 0–2.2 V and −0.6 to 1.2 V for two-electrode and three-electrode systems, respectively. EIS measurements were conducted with an amplitude of 10 mV over a frequency range of 0.1 Hz–10 kHz at OCP.

Equations 1 and 2 were utilized to determine C_S (F g^{-1}) from the CV and GCD data in the three-electrode configuration.[97,98] The capacitance of the graphite sheet was neglected.

$$C_S = \frac{A}{\Delta V \times v \times m} \quad \text{(Equation 1)}$$

$$C_S = \frac{I \times \Delta t}{m \times \Delta V} \quad \text{(Equation 2)}$$

Where, A, ΔV, v, m, Δt and $\frac{I}{m}$ represents the integral area of CV loops, sweep potential window (V), scan rate (V s^{-1}), mass of electrodes (g), discharging time (s) and applied current density (A g^{-1}), respectively.

Equations 3 and 4 were utilized to determine the C_S (F g^{-1}) from the CV and GCD data for the symmetric supercapacitor.[61]

$$C_s = \frac{2A}{\Delta V \times v \times m} \quad \text{(Equation 3)}$$

$$C_s = \frac{2\,(I \times \Delta t)}{m \times V} \quad \text{(Equation 4)}$$

A factor of 2 is introduced to account for the series capacitance that arises in a symmetric supercapacitor device.

Further, the volumetric capacitance (C_V, F cm^{-3}), gravimetric energy density (E_g, Wh kg^{-1}), gravimetric power density (P_g, W kg^{-1}), volumetric energy density (E_V, Wh L^{-1}) and volumetric power density (P_V, W L^{-1}), were calculated according to Equations 5, 6, 7, 8, and 9 respectively:[30]

$$C_V = C_S\,\rho \quad \text{(Equation 5)}$$

$$E_g = \frac{1}{2 \times 4}\,\frac{C_S \times V^2}{3.6} \quad \text{(Equation 6)}$$

$$P_g = \frac{E_g}{\Delta t} \times 3600 \quad \text{(Equation 7)}$$

$$E_V = \frac{1}{2 \times 4}\,\frac{C_V \times V^2}{3.6} \quad \text{(Equation 8)}$$

$$P_V = \frac{E_V}{\Delta t} \times 3600 \quad \text{(Equation 9)}$$

Where, $\rho\left(=\frac{m}{V_{el}}\right)$ represents the density of the material and is calculated by dividing the net mass (g) of the electrode by its volume (V_{el}, cm^{-3}). The thickness of the electrode material was measured using a micrometer (Figure S2).

QUANTIFICATION AND STATISTICAL ANALYSIS

The graphs in both the main text and the supplemental file were generated from raw data using OriginPro 2024b (Learning Edition). SEM images were analyzed with ImageJ, and the area under the CV curves was estimated using OriginPro 2024b (Learning Edition) to calculate the specific capacitance. CV, GCD and EIS measurements were performed using a Metrohm Autolab PGSTAT204 instrument (Metrohm Autolab B.V., Netherlands), operated with the NOVA software package (version 2.1.6).